



LAWRENCE  
LIVERMORE  
NATIONAL  
LABORATORY

LLNL-JRNL-654697

# Simulating x-ray Thomson scattering signals from high-density, millimetre-scale plasmas at the National Ignition Facility

T. Doeppner, D. A. Chapman, D. Kraus, A. L. Kritcher, B. Bachmann, G. W. Collins, R. W. Falcone, J. A. Gaffney, D. O. Gericke, S. H. Glenzer, T. M. Guymier, J. A. Hawreliak, O. L. Landen, S. LePape, T. Ma, P. Neumayer, J. Nielsen, A. Pak, R. Redmer, D. C. Swift, J. Vorberger

May 20, 2014

Physics of Plasmas

## **Disclaimer**

---

This document was prepared as an account of work sponsored by an agency of the United States government. Neither the United States government nor Lawrence Livermore National Security, LLC, nor any of their employees makes any warranty, expressed or implied, or assumes any legal liability or responsibility for the accuracy, completeness, or usefulness of any information, apparatus, product, or process disclosed, or represents that its use would not infringe privately owned rights. Reference herein to any specific commercial product, process, or service by trade name, trademark, manufacturer, or otherwise does not necessarily constitute or imply its endorsement, recommendation, or favoring by the United States government or Lawrence Livermore National Security, LLC. The views and opinions of authors expressed herein do not necessarily state or reflect those of the United States government or Lawrence Livermore National Security, LLC, and shall not be used for advertising or product endorsement purposes.

# Simulating x-ray Thomson scattering signals from high-density, millimetre-scale plasmas at the National Ignition Facility

D.A. Chapman,<sup>1,2,a)</sup> D. Kraus,<sup>3</sup> A.L. Kritcher,<sup>4</sup> B. Bachmann,<sup>4</sup> G.W. Collins,<sup>4</sup> R.W. Falcone,<sup>3</sup> J.A. Gaffney,<sup>4</sup> D.O. Gericke,<sup>2</sup> S.H. Glenzer,<sup>5</sup> T.M. Guymet,<sup>1</sup> J.A. Hawreliak,<sup>4</sup> O.L. Landen,<sup>4</sup> S. Le Pape,<sup>4</sup> T. Ma,<sup>4</sup> P. Neumayer,<sup>6</sup> J. Nilsen,<sup>4</sup> A. Pak,<sup>4</sup> R. Redmer,<sup>7</sup> D.C. Swift,<sup>4</sup> J. Vorberger,<sup>8</sup> and T. Döppner<sup>4</sup>

<sup>1)</sup> *Plasma Physics Group, Radiation Physics Department, AWE plc, Reading RG7 4PR, United Kingdom*

<sup>2)</sup> *Centre for Fusion, Space and Astrophysics, University of Warwick, Coventry CV4 7AL, United Kingdom*

<sup>3)</sup> *Department of Physics, University of California, Berkeley CA 94720, USA*

<sup>4)</sup> *Lawrence Livermore National Laboratory, Livermore CA 94550, USA*

<sup>5)</sup> *SLAC National Accelerator Laboratory, Menlo Park CA 94309, USA*

<sup>6)</sup> *Gesellschaft für Schwerionenforschung, 64291 Darmstadt, Germany*

<sup>7)</sup> *Institut für Physik, Universität Rostock, 18051 Rostock, Germany*

<sup>8)</sup> *Max-Planck-Institut für die Physik komplexer Systeme, 01187 Dresden, Germany*

(Dated: 9 May 2014)

We have developed a model for analysing X-ray Thomson scattering (XRTS) data from large scale, inhomogeneous plasmas created during ultra-high pressure implosions at the National Ignition Facility (NIF) in a spherically convergent geometry. The density weighting of the scattered signal and attenuation of the incident and scattered x-rays throughout the target are included using radial profiles of the density, opacity, ionization state, and temperature from radiation hydrodynamics simulations. Simulations show that the uncollimated scattered signal is strongly weighted toward the bulk of the shocked plasma and the Fermi degenerate material near the ablation front. We show that the scattered signal provides a good representation of the temperature of this highly nonuniform bulk plasma and can be determined to an accuracy of  $\sim 15\%$  using typical data analysis techniques with simple 0D calculations. On the other hand, the mean ionization of the carbon in the bulk is underestimated. We suggest that this discrepancy is due to the convolution of scattering profiles from different regions of the target. Subsequently, we investigate modifications to the current platform to minimise the impact of inhomogeneities, as well as opacity, and also to enable probing of the conditions in the compressed core region.

PACS numbers: 52.25.Os, 52.25.Kn, 52.70.-m

## I. INTRODUCTION

Thomson scattering has been developed over recent years to provide a robust and flexible diagnostic capability for a wide range of experimental conditions pertaining to high power laser-plasma interactions<sup>1-4</sup>, warm dense matter<sup>5-8</sup> studies, laboratory astrophysics<sup>9,10</sup> and inertial confinement fusion (ICF) plasmas<sup>12,13</sup>. Using Thomson scattering, simultaneous measurements of temperature, density and charge balance are made possible by fitting synthetic theoretical spectra to experimental data<sup>14,15</sup>. Naturally, the accuracy of the diagnostic is constrained by many factors, of which the theoretical basis of the underlying physics model is paramount. Intensive development has resulted in significant progress, in the description of, e.g., nonideal and nonequilibrium states as well as geometrical considerations<sup>16-23</sup>.

In this paper, we present a rigorous approach to modelling the spectrum of x-ray Thomson scattering (XRTS) expected from an ongoing series of experiments at the National Ignition Facility (NIF)<sup>24</sup> which aim to mea-

sure the equation of state (EOS) of matter under extreme conditions<sup>25</sup>. Such conditions are challenging to realise experimentally and model theoretically. Measurements in this regime are of great importance for benchmarking and validation of state-of-the-art computational techniques. In these experiments, a series of convergent shocks are utilised in hohlraum-driven, millimetre-scale plastic spheres, creating pressures approaching 1 Gbar at a radius of 50  $\mu\text{m}$  and  $> 1$  Gbar in the core region of the targets upon shock stagnation. Naturally, the passage of such strong shocks leads to highly inhomogeneous plasma conditions throughout the volume illuminated by the probe, significantly complicating the calculation of the expected scattering signal observed by the detector. Furthermore, the transport of the probe through the opacity profile of the dense matter may also influence the shape of the theoretical spectrum.

In order to properly account for such complexities, a high-fidelity numerical model is developed, which directly post-processes radiation-hydrodynamics calculations of the implosion. We find that strong gradients in density, temperature and ionization significantly modify the XRTS spectrum. For example, the width of the inelastic Compton feature becomes highly convoluted due to the contributions of distinct regions of the plasma. We

---

<sup>a)</sup> Electronic mail: david.chapman@awe.co.uk

also account for the transport in 3D of the incident and scattered x-rays via simple ray tracing and show that the shape of the inelastic feature is not significantly affected. On the other hand, we find that the opacity of the target substantially reduces the absolute scattered power and also decreases the ratio of elastic to inelastic scattering.

To investigate the importance of detailed modelling to data analysis, we apply  $\chi^2$  fitting to synthetic data (constructed from our full 3D calculations) based on a simple 0D model. We find that fitting to the Compton feature reproduces the electron density-weighted average temperature to less than 7%, with an uncertainty of ca. 15%. In contrast, the uncertainty of the mean carbon ionization state is only 5%, but yields a fitted value which underestimates equivalent average by 13%. Thus, we demonstrate the importance of detailed modelling of XRTS from highly nonuniform dense plasmas.

## II. GBAR EOS PLATFORM AT NIF

Recently, we reported on the development of an experimental platform to study the EOS of poly( $\alpha$ -methylstyrene) plastic at ultra-high pressures at NIF<sup>25</sup>. The experiments use a platform based on the well-characterised 1D convergent ablator (1D ConA) design developed during the National Ignition Campaign (NIC)<sup>26–28</sup>. The hohlraum is driven by 184 beams in 46 quads with a total energy of 1.3 MJ at a wavelength of 351 nm, yielding radiation temperatures of up to 280 eV. The resulting radiation drive launches a series of four shocks which coalesce in-flight to produce a single strong shock that implodes the plastic sphere. The remaining 8 beams are directed to a 5  $\mu\text{m}$  thick Zn backlighter foil mounted 6 mm from the outer hohlraum wall, producing He- $\alpha$  radiation peaked around 9 keV. Radiation-hydrodynamics simulations using the NIC design code HYDRA<sup>29,30</sup> suggest that pressures in excess of 1 Gbar are reached upon shock convergence (see Fig. 1(a)), with densities and temperatures approaching 40  $\text{g cm}^{-3}$  and 2 keV, respectively.

The implosions are diagnosed using streaked x-ray radiography and also scattering of the backlighter probe. The radiography is used to determine the shock speed, mass density and opacity profiles via a novel profile matching technique<sup>35</sup>. The pressure at the shock front is then inferred from the Rankine-Hugoniot relations. The XRTS measurement is made after peak compression using a specially designed mono-angle crystal spectrometer (MACS)<sup>36</sup> with a temporal resolution of  $\sim 100$  ps, resulting in a well-defined scattering angle of  $\vartheta = 84.5^\circ$  which accesses the non-collective response of the plasma. Thus, the shape of the downshifted inelastic feature provides a direct measurement of the momentum distribution of the electrons<sup>31</sup>. For the non-degenerate states we expect to create, such a measurement is directly correlated with the plasma temperature. Furthermore, information on the mean ionization state is attainable via the ratio of

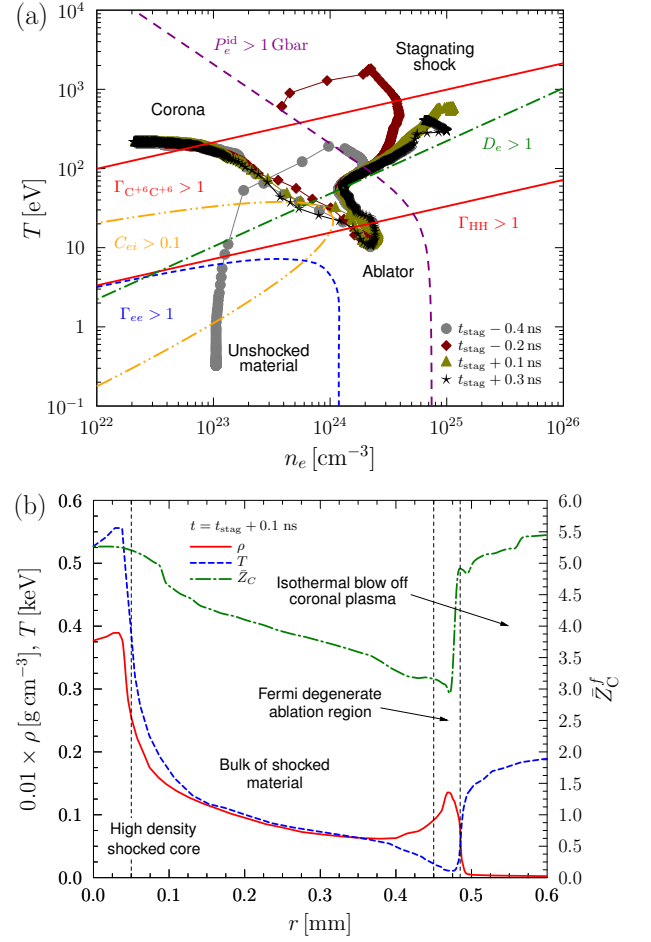


FIG. 1. (Colour online) (a): Cell trajectories from 1D HYDRA calculation on the  $n_e$ - $T$  plane for several times pre- and post-stagnation time,  $t_{\text{stag}}$ . Contours for the coupling parameters,  $\Gamma_{aa} = \langle V_{aa} \rangle / \langle K_a \rangle = 1$ , for the ions (solid red) and electrons (dashed blue), electron degeneracy parameter,  $D_e = n_e \Lambda_e^3 = 1$ , (dot-dashed green) and electron-ion collision parameter,  $C_{ei} = \nu_{ei} / \omega_{pe} = 0.1$ , (dash-double dotted orange) are shown. States achieving an ideal electron pressure  $P_e^{\text{id}} > 1$  Gbar (long dashed purple) occur in the centre of the target after shock convergence. (b): Radial mass density (solid red), temperature (dashed blue) and ionization profiles (dash-dotted green) immediately after shock stagnation,  $t = t_{\text{stag}} + 0.1$  ns, show several distinct regions and strong gradients produced during the implosion.

elastic to inelastic scattering.

Previously XRTS experiments have been focused on probing a relatively homogeneous volume of plasma throughout the duration of the measurement<sup>14,32–34</sup>. This has made data analysis using 0D codes, which consider only a single set of plasma conditions as inputs, reasonably robust. If, however, we wish to probe a plasma that is driven out of equilibrium<sup>37,38</sup>, probed on ultra-short time scales<sup>22,39,40</sup> or produced with strong gradients in the sampled volume<sup>10</sup>, significant difficulties in interpreting the scattered signal can arise.

Relative to the rapid equilibration time of the shocked matter<sup>11</sup>, the hydrodynamic evolution of the target is sufficiently slow for the plasma to be locally treated in equilibrium, although convergence effects lead to strong radial plasma gradients over large scale lengths. Figure Fig. 1(b) shows several distinct regions which are produced by the passage of the shock, which persist throughout the duration of the backlighter. Specifically, the Gbar states of interest occur in a high-density, hot core of radius  $\lesssim 50 \mu\text{m}$ , surrounded by a larger bulk of shocked plasma at  $8\times$  compression and around 100 eV. In the ablator shell, the density profile peak exceeds  $12\times$  compression whilst remaining at low ( $\sim 10$  eV) temperature due to the low adiabat implosion provided by the four-shock pulse shape. Outward, a quasi-isothermally expanding corona of high temperature, low density blow-off plasma envelops the target. Since the scattering spectrometer views the entire target through the upper LEH, the observed XRTS spectrum will reflect the total spatially-integrated scattering from this highly inhomogeneous plasma.

### III. THEORETICAL DESCRIPTION OF X-RAY THOMSON SCATTERING SIGNALS FROM INHOMOGENEOUS MULTICOMPONENT PLASMAS

Thomson scattering from inhomogeneous plasmas has previously been considered in high temperature laser-produced plasmas probed with optical<sup>41,42</sup> and UV<sup>43</sup> lasers, optically-pumped XUV sources<sup>44</sup>, and WDM probed with soft x-ray free electron lasers<sup>45</sup>. In all cases, significant effects on the shape of the excitation spectrum for both ion acoustic and plasmon modes have been shown to result from gradients in the plasma conditions<sup>46,47</sup>. In dense, high-opacity samples the attenuation of the probe due to bound-free transitions and photoionization must also be considered<sup>48</sup>.

In general, the differential power spectrum of radiation scattered by an inhomogeneous volume of plasma,  $\mathcal{V}$ , as observed by a spatially integrating detector is given by

$$\frac{\partial^2 P_s(\mathbf{k}, \omega)}{\partial \Omega \partial \omega} \propto \int_{\mathcal{V}} d\mathbf{r} \bar{n}_i(\mathbf{r}) \frac{\partial^2 \sigma(\mathbf{k}, \omega; \mathbf{r})}{\partial \Omega \partial \omega} * I(\omega, \mathbf{r}), \quad (1)$$

in terms of the energy and momentum shifts  $\hbar\omega = \hbar\omega_i - \hbar\omega_s$  and  $\hbar\mathbf{k} = \hbar\mathbf{k}_i - \hbar\mathbf{k}_s$ , respectively. Here, the  $*$  symbol denotes convolution in the frequency domain.

The range of wave numbers probed over the range of the spectrometer is  $k = (k_s^2 + k_i^2 - 2k_s k_i \cos \vartheta)^{1/2}$ , where the scattering angle  $\vartheta$  is determined by the experimental geometry. Dispersion of the x-rays at a given point in the sample can be approximately accounted for via  $k_{i,s}(\mathbf{r}) = (\omega_{i,s}^2 - \omega_{pe}^2(\mathbf{r}))^{1/2}/c$ , where  $\omega_{pe}(\mathbf{r}) = (e^2 n_e(\mathbf{r})/\varepsilon_0 m_e)^{1/2}$  is the local plasma frequency.

The double-differential cross section describing the probability of scattering the incident photons,  $\partial^2 \sigma(\mathbf{k}, \omega; \mathbf{r})/\partial \Omega \partial \omega$ , is weighted by the mean ion density

distribution,  $\bar{n}_i(\mathbf{r})$ , and convolved with the local x-ray intensity profile,  $I(\omega, \mathbf{r})$ . The cross section is given by<sup>49</sup>

$$\frac{\partial^2 \sigma(\mathbf{k}, \omega; \mathbf{r})}{\partial \Omega \partial \omega} = \sigma_T (\omega_i/\omega_s)^2 \bar{Z}_A(\mathbf{r}) S_{ee}^{\text{tot}}(\mathbf{k}, \omega; \mathbf{r}), \quad (2)$$

where  $\sigma_T = 6.65 \times 10^{-29} \text{ m}^2$  is the Thomson scattering cross section for a single electron,  $\bar{Z}_A(\mathbf{r})$  is the local mean atomic number of the plasma and  $S_{ee}^{\text{tot}}(\mathbf{k}, \omega; \mathbf{r})$  is the local total dynamic structure factor (DSF) of the electrons.

The DSF describes the microscopic spatio-temporal correlations between all the electrons in the fully coupled many-body system. For partially ionized, multi-component plasmas probed with x-rays the well-known expression due to Chihara<sup>50</sup> is generalised according to

$$\bar{Z}_A S_{ee}^{\text{tot}}(\mathbf{k}, \omega) = W_R(k) \delta(\omega) + W_C(\mathbf{k}, \omega), \quad (3)$$

in which the weights of the elastic ‘Rayleigh’ scattering term is<sup>20,51</sup>

$$W_R(k) = \sum_{ab} \sqrt{x_a x_b} [f_a(k) + q_a(k)] [f_b(k) + q_b(k)] S_{ab}(k), \quad (4)$$

and the inelastic ‘Compton’ term is

$$W_C(\mathbf{k}, \omega) = \sum_a x_a Z_a^f S_{ee}^0(\mathbf{k}, \omega) + \sum_a x_a Z_a^b \tilde{S}_{ae}(\mathbf{k}, \omega). \quad (5)$$

Here,  $x_a = n_a/\sum_a n_a$  are the concentrations of ion species  $a$  and  $Z_a^f$  and  $Z_a^b$  are the numbers of free and bound electrons per ion, respectively. The mean ionization of the plasma is then  $\bar{Z}_i^f = \sum_a x_a Z_a^f$ .

The Rayleigh feature (4) contains contributions due to scattering from electrons in tightly bound states and also the screening cloud which dynamically follows the ions. The Fourier densities of these terms are given by  $f_a(k)$  and  $q_a(k)$ , respectively and are modulated by the static ion-ion structure factors  $S_{ab}(k)$ . In contrast, the Compton feature (5) corresponds to inelastic scattering from free electrons,  $S_{ee}^0(\mathbf{k}, \omega)$ , and also Raman-like transitions from bound states into the continuum,  $\tilde{S}_{ae}(\mathbf{k}, \omega)$ .

Note that in Eqs. (3 - 5) the ions have been treated statically, such that their dynamical behaviour is described by a  $\delta$ -function. Such a treatment is reasonable since collective excitations of the ions (acoustic waves)<sup>52,53</sup> cannot currently be resolved by our spectrometer.

### IV. VIXEN NUMERICAL MODEL

By using radiation-hydrodynamics simulations to directly inform our calculations, we are able to produce high fidelity predictions of the expected scattering signal which may be used for forward modelling and benchmarking. We refer to our approach as VIXEN: Volume-Integrated X-ray scattering for Experiments with Non-uniform plasmas.

We consider a CH plasma in thermal equilibrium composed of electrons and equal number densities of hydrogen and carbon ions; the Ge doping of preheat shielding layer (1% by number density)<sup>25</sup> is not expected to be negligible. The hydrogen is assumed to be fully ionized whereas the carbon ionization is found from  $\bar{Z}_C^f = 2\bar{Z}_i^f - 1$ , where  $\bar{Z}_i^f$  is the mean ionization as calculated in HYDRA using the OPAL model<sup>54</sup>. Two adjacent charge states of carbon are further considered in order to fulfil electroneutrality, with  $Z_C^{f0} = \text{floor}(\bar{Z}_C^f)$  and  $Z_C^{f1} = Z_C^{f0} + 1$ , which are treated as distinct species. The corresponding densities are given by  $n_C^0 = (1 - \zeta)n_C$  and  $n_C^1 = \zeta n_C$ , where  $\zeta = \bar{Z}_C^f - Z_C^{f0}$ .

Although partitioning the mean carbon ionization into two adjacent states is amenable for coupling our XRTS calculations to the HYDRA output, it is *not* a realistic description of the true charge distribution in the plasma. Thus, some error in the description of ion-ion correlations and the contribution of specific bound states to the DSF may be introduced. Improving the description of the carbon charge state distribution via, e.g. detailed configuration accounting, is beyond the scope of the present work, but could potentially be incorporated using our general multicomponent framework.

### A. Dynamic structure factor

The free-free component (first term in Eq. (5)) follows from the fluctuation-dissipation theorem<sup>55</sup> in terms of the density response function. For weakly coupled plasmas, the latter may be evaluated in random phase approximation (RPA), whereas strong coupling in the electronic subsystem and collisions with the ions can be incorporated within an extended Mermin approach<sup>17,56</sup>. From the trajectories shown in Fig.1(a) an RPA treatment is reasonable since the plasma remains weakly coupled ( $\Gamma_{ee} \ll 1$ ) and effectively collisionless ( $C_{ei} \ll 1$ ) following shock stagnation. Moreover, for non-collective scattering, i.e. for large  $k$ , the DSF of the free electrons,  $S_{ee}^0(\mathbf{k}, \omega)$ , is not sensitive to modifications of the dynamic screening due to local field corrections. Probing at large  $k$  also allows bound-free transitions to be reliably described within the impulse approximation (IA)<sup>57–59</sup>. In particular, transitions from the L-shell are well-described, whereas K-shell excitations do not significantly overlap with the free-free feature<sup>60</sup>. Thus, the description of the total inelastic scattering is expected to be robust.

Conversely, the ions remain strongly coupled ( $\Gamma_{ii} \gtrsim 1$ ) after the shock, which affects the strength of the elastic scattering via the partial ion structure factors,  $S_{ab}(k)$ . The Rayleigh amplitude therefore represents a potentially large source of uncertainty for estimates of the ionization balance. Strongly correlated multicomponent ionic systems can be accurately modelled within the generalised hypernetted-chain approximation<sup>18</sup>, which has been extensively validated against first-principles density functional molecular dynamics<sup>61</sup>.

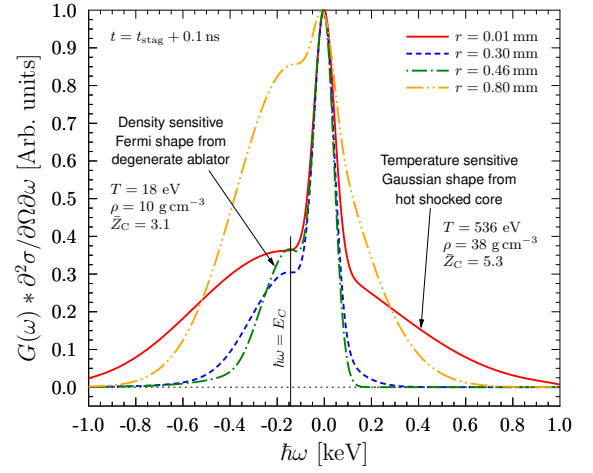


FIG. 2. (Colour online) Lineouts of the differential scattering cross section,  $\partial^2 \sigma / \partial \Omega \partial \omega$ , convolved with a Gaussian profile  $G(\omega)$  as a function of scattered energy  $\hbar \omega_s$  for various radii of interest after peak compression. The vertical line marks the Compton energy  $E_C = \hbar^2 k^2 / 2m_e$  for the wave number probed by our experiment.

The form factors of the tightly bound electrons,  $f_a(k)$ , can be obtained to high accuracy for ionized, low- $Z$  materials<sup>62</sup> and, moreover, the screening cloud,  $q_a(k)$ , has recently been investigated for conditions relevant to our experiment<sup>63,64</sup>. Once again, probing at large  $k$  lessens the uncertainty due to modelling since the partial structure factors are close to their ideal plasma values ( $S_{a=b} = 1$  and  $S_{a \neq b} = 0$ ) and the screening cloud is a small correction to the bound electron form factors.

In Fig. 2, the radial dependence of the scattering profile is shown in each of the distinct regions of the target (see Fig. 1(b)) immediately after peak compression. Here, the spectral shape of the x-ray source, which controls the shape of the elastic feature and broadens the inelastic feature, is approximated using a Gaussian function  $G(\omega) = (\pi \omega_0^2)^{-1/2} \exp(-\omega^2 / \omega_0^2)$  with characteristic width  $\hbar \omega_0 = 100$  eV.

Clear differences in the total scattering signal from each region can be seen. The stagnation of the shock in the core ( $r \lesssim 0.05$  mm) yields high densities and temperatures and near full ionization, resulting in a broad Compton feature due mostly to free-free scattering. The strong Rayleigh signal from the core is attributable to the large scale length of the screening cloud around the near-fully ionized carbon ions, which dominates the elastic scattering.

In the bulk of the shocked material surrounding the compressed core ( $r \sim 0.05$ – $0.45$  mm) the steady decay of the temperature profile is reflected by the significantly less broadened Compton peak. Moreover, for much of the bulk region the K-shell of the carbon remains fully bound, leading to a small red-shifted tail on the Compton peak due to bound-free transitions and also a strong enhancement of the Rayleigh scattering intensity.



In contrast, the weakly heated material behind the ablation front ( $r \sim 0.46$  mm) yields a Compton feature whose shape is determined by the free electron density rather than the temperature, reflecting the transition from Maxwell-Boltzmann to Fermi-Dirac statistics for degenerate matter. Moreover, in addition to a pronounced K-shell bound-free feature, a significant contribution due to scattering from bound L-shell states is also present around the Compton energy,  $E_C$ . Relative to the bulk of the plasma, the elastic scattering intensity of the ablator material decreases since there are fewer free electrons screening the ions and also due to the shorter screening length of the degenerate system. Note that the additional bound L-shell electrons present in the ablator region do not meaningfully contribute to elastic scattering at the large wave numbers accessed by the probe.

Lastly, the shape of the spectrum from the hot, diffuse coronal blow-off plasma ( $r \gtrsim 0.5$  mm) shows a strong temperature dependent Compton peak, dominated by free-free scattering, as expected. Conversely to the core region, here the total elastic contribution is significantly weaker since the screening cloud contribution falls off with the exponential decay of the density profile.

## B. X-ray attenuation

In addition to the cross section described by Eq. (2), the density and intensity profiles also contribute to the spatial dependence of the scattered power spectrum (1). In particular, the spatial variation of the intensity accounts for both the source profile and also the dependence of the plasma opacity on the temperature and density profiles. Thus, the photon flux at a given point in the target is affected by the transport of the x-rays, which can be followed by ray tracing. Such a scheme was recently reported by Golovkin *et al.* in which XRTS calculations<sup>14</sup> were integrated into the SPECT3D code<sup>23</sup>, allowing the effects of plasma gradients and  $k$ -blurring on the scattering spectrum to be systematically investigated.

In the present experiment, the large scale of the NIF hohlraum means that the distance from the target to both the backlighter foil and the detector are much larger than its characteristic size and, thus, the x-ray source can be reliably treated as parallel rays scattering through a constant angle of  $\vartheta = 84.5^\circ$ , i.e. source divergence is not important. Furthermore, the opacity varies only weakly with frequency over the detection range of our spectrometer ( $\sim 7.5$ – $10$  keV), such that a single channel (centred on 9 keV) is sufficient for our calculations.

Considering the opacity at only a single frequency also serves to significantly simplify our model as the source spectrum does not need to be modified as it propagates through the target. Subsequently, the intensity profile can be separated into

$$I(\omega, \mathbf{r}) = I_0 \Sigma(\omega) \mathcal{P}(\mathbf{r}) \mathcal{A}(\mathbf{r}), \quad (6)$$

where  $I_0$  is the peak intensity,  $\Sigma(\omega)$  and  $\mathcal{P}(\mathbf{r})$  represent

the spectral shape and spatial profile of the emission from the backlighter foil, respectively, and  $\mathcal{A}(\mathbf{r})$  represents the weight of a given point in the target due to the attenuation of both the incident and scattered photons, as seen by the detector.

The geometry of our model uses a coordinate system rotated from that of the NIF target chamber such that the scattering is in the  $x$ - $y$  plane with the x-ray source in the  $x$ - $z$  plane. The calculation of the integrand of Eq. (1) over the full 3D volume of the simulation is constructed tomographically by iterating 2D calculations in the scattering plane over  $z$ . Combining Eqs. (1 - 6) the total scattered power can be written

$$\frac{\partial^2 P_s^{3D}}{\partial \Omega \partial \omega} \propto \sigma_T I_0 \int_{-R}^R dz \int_{-R}^R dy \int_{-R}^R dx \mathcal{W}(x, y, z) \times [\mathcal{S}_R(k, \omega; r_{xyz}) + \mathcal{S}_C(\mathbf{k}, \omega; r_{xyz})]. \quad (7)$$

In Eq. (7),  $R = 1$  mm is the radius of the target in the HYDRA calculation, and we have defined

$$\mathcal{S}_R(k, \omega) = \Sigma(\omega) W_R(k), \quad (8)$$

$$\mathcal{S}_C(\mathbf{k}, \omega) = \Sigma(\omega) * [(\omega_i/\omega_s)^2 W_C(\mathbf{k}, \omega)]. \quad (9)$$

The total weight of the scattering signal from a point in the target is defined as

$$\mathcal{W}(x, y, z) = \rho(r_{xyz}) \mathcal{P}(x, z) \mathcal{A}(x, y, z). \quad (10)$$

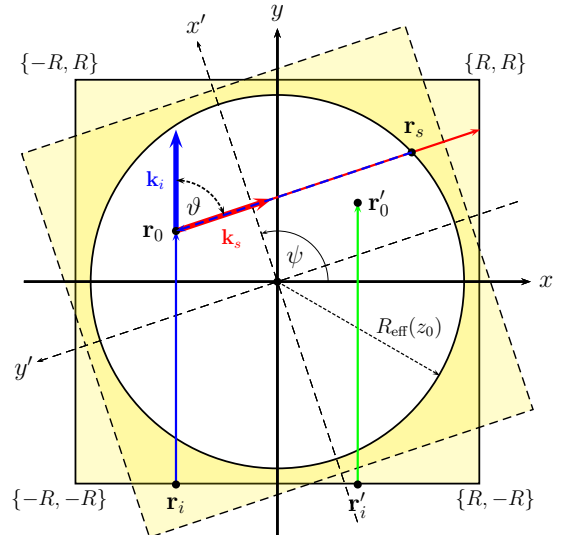


FIG. 3. (Colour online) Graphical representation of x-ray attenuation calculations performed in VIXEN in the plane with elevation  $z_0$ . The paths of incident (thin blue vector) and scattered (thin red vector) rays are shown. The attenuation on the path  $\mathbf{r}_0 \rightarrow \mathbf{r}_s$  is identical to that experienced by an incident ray propagating in reverse (dashed thin blue vector). Under coordinate rotation this is also equivalent to the attenuation along the path  $\mathbf{r}'_i \rightarrow \mathbf{r}'_0$  (thin green vector). The shaded regions contain no data from the HYDRA simulation since  $r_{xyz} > R_{\text{eff}}(z_0) = (R^2 - z_0^2)^{1/2}$  and are assumed to be perfectly transmissive.

For simplicity, it is convenient to consider the case of uniform illumination, i.e.  $\mathcal{P}(x, z) = 1$ .

The radially symmetric density profile and scattering contributions  $\mathcal{S}_R$  and  $\mathcal{S}_C$  are easily interpolated into the Cartesian simulation space using  $r_{xyz} = (x^2 + y^2 + z^2)^{1/2}$ , with  $\mathcal{W}(x, y, z) = 0$  for  $r_{xyz} > R$ . Conversely, the attenuation term is, in general, a complicated function of position in the 3D volume. We decompose it into the product  $\mathcal{A}(x, y, z) = \mathcal{A}^{\text{in}}(x, y, z) \times \mathcal{A}^{\text{sc}}(x, y, z)$ , where the first term corresponds to the attenuation of incident parallel rays moving into the target in the scattering plane and the second term gives the attenuation of the scattered rays as seen from the detector.

Figure 3 illustrates the method by which the transport and propagation of the probe are considered. Here, an incident ray is shown propagating from a point on the rear boundary of the simulation box  $\mathbf{r}_i = \{x_0, -R, z_0\}$  along the  $y$ -direction to a point of interest in the target  $\mathbf{r}_0 = \{x_0, y_0, z_0\}$ . The cumulative attenuation experienced by photons along this path is given by the Beer-Lambert law

$$\mathcal{A}^{\text{in}}(x_0, y_0, z_0) = \exp \left[ - \int_{-R}^{y_0} dy \rho(r_{x_0 y z_0}) \kappa(r_{x_0 y z_0}) \right], \quad (11)$$

where  $\kappa$  is the local opacity at  $\hbar\omega = 9 \text{ keV}$ .

Subsequently, the ray is scattered from  $\mathbf{r}_0$  toward the detector, exiting the plasma at  $\mathbf{r}_s$ , and is further attenuated. Since the HYDRA simulations are radially symmetric, then from the perspective of the detector the weight of  $\mathbf{r}_0$  is decreased by a fraction equivalent to that of an incident ray propagating in reverse from a virtual source at the detector (see Fig. 3). Thus, the attenuation of the scattered ray can be found by a coordinate rotation, i.e.  $\mathcal{A}^{\text{sc}}(x, y, z) = \mathcal{A}^{\text{in}}(x', y', z)$ , where  $x' = x \cos \psi + y \sin \psi$  and  $y' = -x \sin \psi + y \cos \psi$ , with the angle of rotation  $\psi = \pi - \vartheta$ .

### C. 3D weighting distributions

Multiplying the total attenuation by the density profile and iterating the calculation illustrated in Fig. 3 over all  $z$  in the simulation space builds a 3D map of the total weighting function throughout the target. Fig. 4(a) shows a three-slice through  $\mathcal{W}(x, y, z)$  immediately after shock stagnation. In this image the x-ray probe is incident from the right and is scattered through a uniform angle at every point toward a detector located above the simulation space (in the positive  $x$  direction).

A contour map of the scattering ( $x$ - $y$ ) plane for  $z = 0$  is shown in Fig. 4(b). The thin white region (for references to colour the reader is referred to the online article) on the detector-facing hemisphere of the illuminated side of the target (upper right quadrant) corresponds to the high-density material just behind the ablation front. The high weight of this region reflects the short overall path length the x-rays take through low-opacity plasma

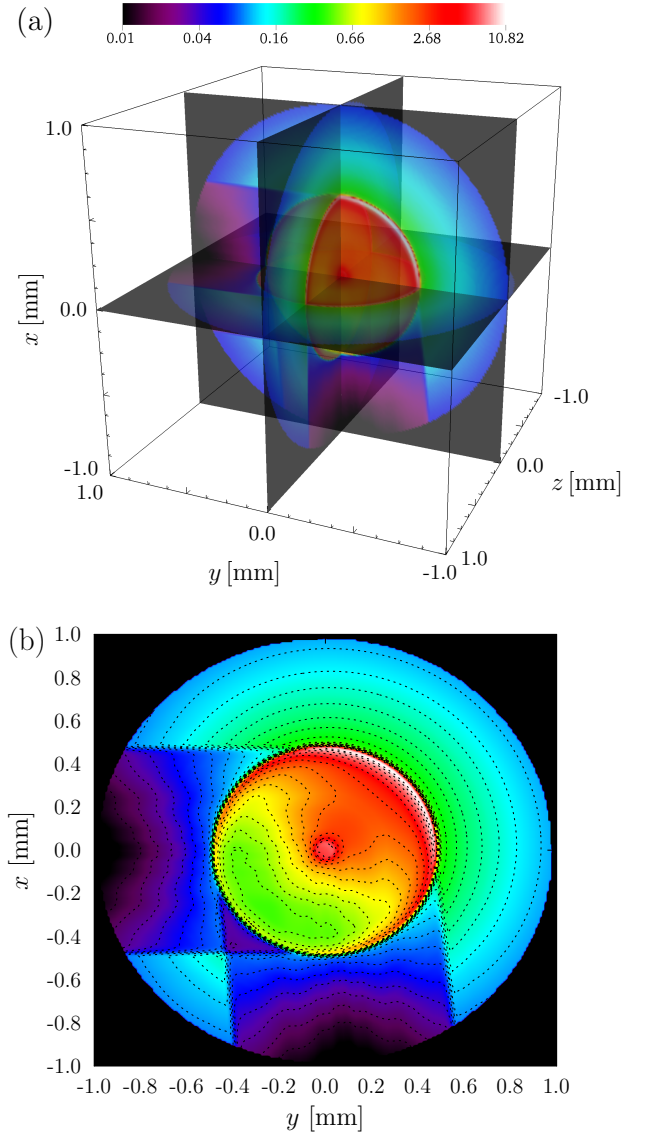


FIG. 4. (Colour online) (a): 3D view of the total weighting function,  $\mathcal{W}(x, y, z)$ , of a uniformly illuminated target ( $\mathcal{P}(x, z) = 1$ ) due to both attenuation and density immediately following shock stagnation  $t = t_{\text{stag}} + 0.1 \text{ ns}$ . (b): 2D slice through the scattering ( $x$ - $y$ ) plane at  $z = 0$ . The colour scale indicates regions contributing low (black-purple) and high (red-white) weight to the Cartesian integration in Eq. (7) and is the same in both plots.

and also its high density weighting. A region at smaller radii with relatively high weight is also present in the same quadrant, corresponding to scattering from the rebounding shock front. Conversely, the coronal plasma contributes only a very small proportion to the total scattering. This is entirely due to the low density weighting of the blow-off plasma since its opacity is negligible.

The effect of the opacity of the compressed target is manifest in the asymmetry of the weighting function with respect to the illuminated and unilluminated sides of the target, with a strong ‘shadow’ being cast behind the ball



from the perspectives of both the x-ray source and the detector. The strength of the shadow also notably increases following shock convergence as the opacity of the core reaches a maximum.

## V. RESULTS

Having calculated the spatial dependence of the components of the scattering spectrum and the weighting function, the 3D integration is straightforward to perform. Thus, plasma inhomogeneities and the transport of the probe x-rays throughout the target can be rigorously accounted for in the expected signal from our experiment. Figure 5 shows the spatially integrated scattered power according to Eq. (7) during the stagnation phase and subsequent rebound of the shock. The spectral shape of the backlighter (see inset) has been taken from measurements of Zn He- $\alpha$  emission from laser-driven brass foils at the Omega laser<sup>65</sup>.

Clearly, the spectral shape of the spatially-integrated power spectrum does not significantly change during shock stagnation. Specifically, post-stagnation the spectrum does not show any noticeable enhancement of the red-shifted wing of the Compton feature, as would be expected for the high temperature, nondegenerate states created in the compressed core. This behaviour is readily understandable via the 3D weighting distributions; the dominant contributions to the signal come from the large volume of bulk plasma and the shell of high-density material in the ablator, both of which remain in quasi-steady states throughout the simulation. In these regions the carbon is relatively weakly ionized,  $\bar{Z}_C^f = 3-4$ , meaning that bound electrons play an important role. The lack of evolution of the spectral shape with the plasma conditions is therefore also partly due to the theoretic-

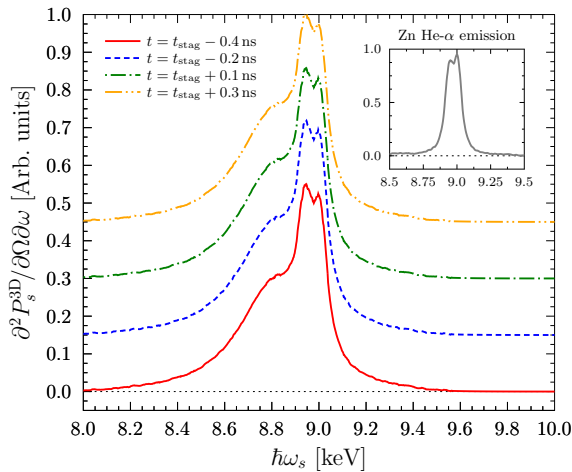


FIG. 5. (Colour online) Time evolution of the total spatially integrated scattered power spectrum between  $t_{\text{stag}} - 0.4$  ns and  $t_{\text{stag}} + 0.3$  ns for a typical Zn He- $\alpha$  source (inset). Successive times are artificially offset in the  $y$ -axis.

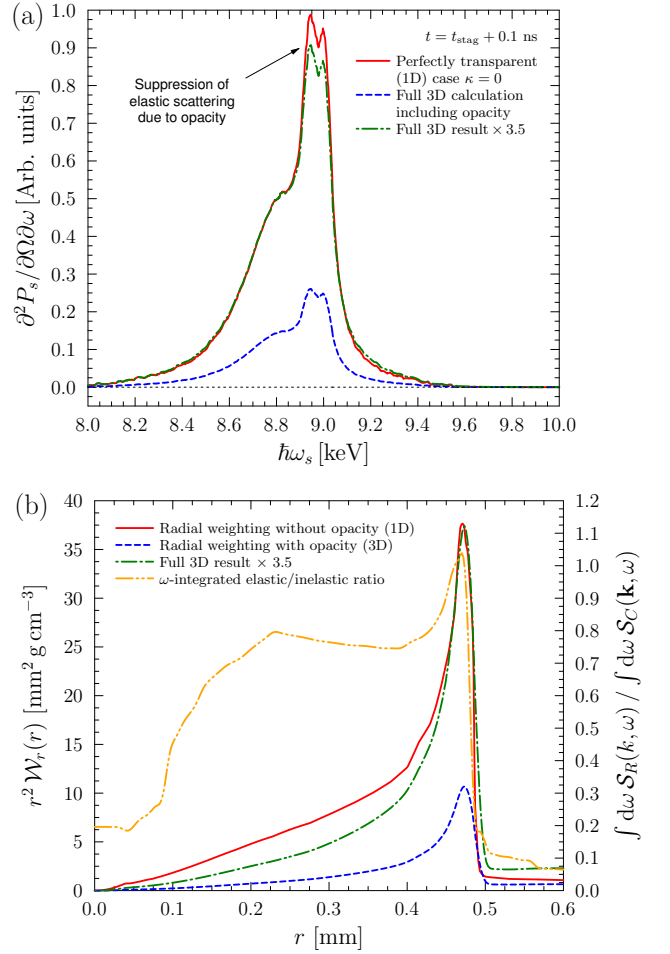


FIG. 6. (Colour online) (a): Comparison of VIXEN calculations without (solid red) and with (dashed blue) x-ray attenuation due to the opacity profile of the target. Scaling the calculation including opacity (dot-dashed green) reproduces the shape of the Compton feature for the perfectly transparent case, but not the relative amplitudes of the Rayleigh and Compton peaks. (b): Angularly averaged weighting function as a function of radius for the same time as panel (a). The elastic/inelastic scattering ratio is also plotted.

cal models presently used to describe the contributions bound electrons; the ionic form factors,  $f_C(k)$ , and the dynamic bound-free terms  $\tilde{S}_{Ce}(\mathbf{k}, \omega)$ , are insensitive to changes in the temperature and density.

### A. Importance of opacity

The significance of the role played by accounting for attenuation of the x-rays on the total scattered signal can be gauged by comparing our results to calculations in which the opacity is set to zero. In this case, Eq. (7) can be re-written in terms of a 1D radial integration (once

more assuming uniform illumination, i.e.  $\mathcal{P} = 1$ )

$$\frac{\partial^2 P_s^{1D}}{\partial \Omega \partial \omega} \propto \sigma_T I_0 \int_0^R dr r^2 4\pi \rho(r) \times [\mathcal{S}_R(k, \omega; r) + \mathcal{S}_C(\mathbf{k}, \omega; r)]. \quad (12)$$

At peak compression, where the opacity of the target is highest, we find the absolute intensity of the full 3D calculation is reduced by a factor of  $\sim 3.5$  compared to the 1D ( $\kappa = 0$ ), completely transparent estimate, as shown in Fig. 6(a).

Another potentially significant consequence of the opacity can be seen when the 3D result is scaled to reproduce the height of the Compton feature of the 1D calculation. Although the shape of inelastic peak is negligibly affected, we find that the ratio of elastic to inelastic scattering is anomalously reduced by ca. 10% when x-ray attenuation is accounted for. Integrating the total weighting factor of the 3D calculation,  $\mathcal{W}(x, y, z)$ , over all angles  $\theta$  and  $\phi$  gives an average radial weighting factor

$$\mathcal{W}_r(r) = \int_0^{2\pi} d\phi \int_0^\pi d\theta \sin \theta \mathcal{W}(x, y, z). \quad (13)$$

Comparing the above to the perfectly transparent case (which gives  $\mathcal{W}_r(r) = 4\pi \rho(r)$ ), and additionally weighting by  $r^2$  for the cell volume scaling, shows a strong relative decrease (see Fig. 6(b)) in the mean radial weighting of the inner parts of the target due to attenuation.

Plotting the ratio of the frequency-integrated total elastic and inelastic scatter shows a large peak in the ablator at  $r = 0.47$  mm, where the shape of the radial weighting is, on average, not heavily influence by attenuation. Naturally, here the scaled 3D radial weighting agrees well with the 1D case. A second, broader peak can also be seen between  $0.15 \lesssim r \lesssim 0.4$  mm, which arises due to the scaling of the screening cloud with the increasing temperature toward the core. Note that the latter is, however, only a small correction to the temperature and density-independent structure of the K-shell, which is the dominant contribution to the Rayleigh scattering amplitude at large  $k$  for weakly ionized states. Indeed, the peak begins to abruptly drop for  $r < 0.22$  mm, where  $Z_C^f \geq 4$ , as the elastic scattering is K-shell begins to ionize. Clearly, the relative weighting of this region is prominently reduced when opacity effects are considered. Thus, the uncertainty of XRTS measurements of the mean ionization state using the ratio of elastic to inelastic scattering may be larger than anticipated if opacity effects are not accounted for.

## VI. SYNTHETIC DATA FITTING

Finally, we briefly investigate the applicability of typical data analysis methods to the proposed experiments using the technique of  $\chi^2$ -minimisation<sup>66,67</sup>. Synthetic data sets representative of the XRTS signal we expect

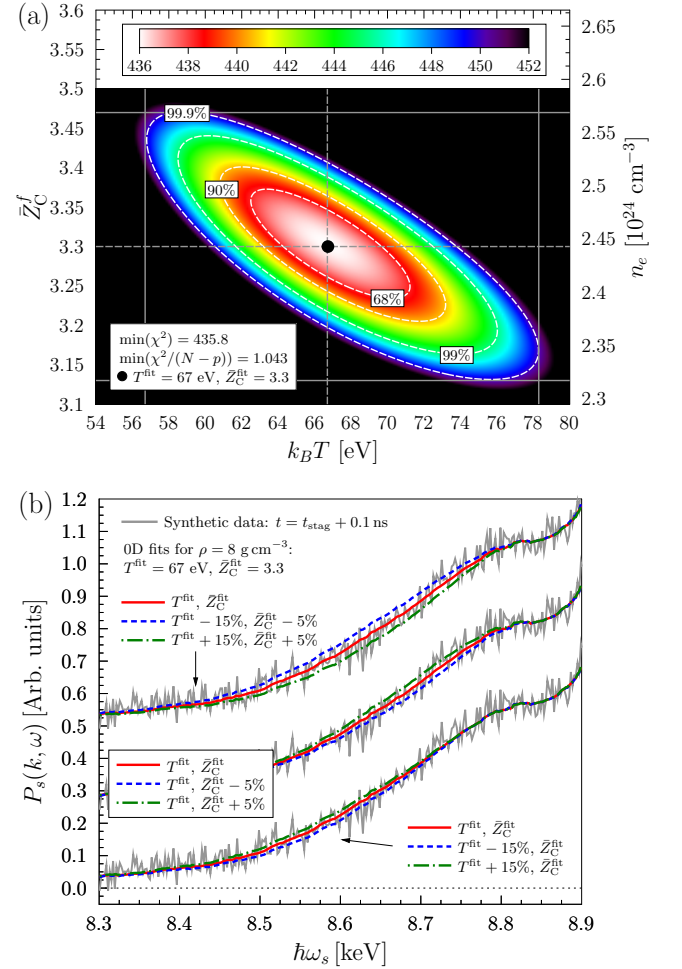


FIG. 7. (Colour online) (a)  $\chi^2$  goodness of fit metric between synthetic experimental data and 0D calculations, as a function of temperature and carbon charge state for  $8 \text{ g cm}^{-3}$ . (b) Comparison of synthetic scattering signal (noisy solid grey curve) to 0D calculations at the best fit conditions (solid red) and with variations to  $T$  (lower set of curves) and  $Z_C$  (upper set of curves) within the limits of the estimated uncertainties.

to observe in our experiment are produced by adding an appropriate level of random normally-distributed noise to the 3D-integrated VIXEN calculations. The resulting noisy scattering profile is then fitted using 0D calculations, i.e. calculations of the scattered power spectrum for a single set of input conditions  $\{Z_C^f, T, \rho\}$ , based on the core physics model of the VIXEN code

$$\frac{\partial^2 P_s^{0D}}{\partial \Omega \partial \omega} \propto \sigma_T I_0 \mathcal{V} \rho [\mathcal{S}_R(k, \omega) + \mathcal{S}_C(\mathbf{k}, \omega)]. \quad (14)$$

Note that similarly to the 1D approach, Eq. (12), the attenuation of the probe is not taken into account in the 0D model.

The  $\chi^2$  parameter<sup>68</sup> is calculated between the 0D calculations and synthetic data over a range of carbon charge states and temperatures. The range of energies over which the fit is performed is limited to the Comp-

ton peak,  $8.3 \leq \hbar\omega_s \leq 8.85$  keV. This is done to mitigate both model uncertainties in the description of the Rayleigh weight and opacity effects, which we have shown to primarily affect the elastic scattering amplitude (see Fig. 6(a)). Instead,  $W_R(k)$  is constrained to reproduce the ratio of inelastic to elastic scattering given by the input 3D VIXEN calculation over the whole  $\bar{Z}_C^f - T$  space. Decomposing elastic and inelastic contributions via the Chihara formula (3) one finds an ‘ideal’ Rayleigh weight

$$W_R(k) = \frac{\mathcal{R} \mathcal{S}_C(\mathbf{k}, \omega_C) - \mathcal{S}_C(\mathbf{k}, \omega_i)}{\Sigma(\omega_i) - \mathcal{R} \Sigma(\omega_C)}, \quad (15)$$

where  $\mathcal{R}$  is the relative amplitude of the input 3D VIXEN calculation at the incident x-ray frequency  $\omega_i$  and Compton frequency  $\omega_C$ .

The input mass density is not varied in the fitting procedure since the density profile will be obtained independently from analysis of the radiographic data in our experiments. Within the accuracy of the radiography analysis an uncertainty in the mass weighted density can be conservatively given as  $\delta\langle\rho\rangle_{\text{elec}}/\langle\rho\rangle_{\text{elec}} = 7.5\%$ . Changes to the input density on this level result in marginal changes to the location of the best fit. Thus, we expect that the main uncertainty in temperature and ionization measurements using XRTS will come from the fitting procedure itself.

Since the x-ray scattering intensity is weighted toward regions with greater numbers of electrons (free and bound), the appropriate conditions against which the 0D fitting results should be compared are the total electron density-weighted averages predicted by the HYDRA simulations

$$\langle X \rangle_{\text{elec}} = \frac{\int_0^R dr 4\pi r^2 n_e^{\text{tot}}(r) X(r)}{\int_0^R dr 4\pi r^2 n_e^{\text{tot}}(r)}. \quad (16)$$

Here,  $X(r)$  stands for the plasma parameter profiles of interest, i.e. temperature and carbon charge state, and the total electron density is  $n_e^{\text{tot}} = \bar{Z}_A \bar{n}_i$ .

Figure 7(a) shows the  $\chi^2$  goodness of fit metric as a function of the temperature and mean carbon ionization. The electron density-weighted average mass density of the target following peak compression is  $\langle\rho\rangle_{\text{elec}} = 8 \text{ g cm}^{-3}$ . A global minimum is clearly present, yielding  $T^{\text{fit}} = 67 \text{ eV}$  and  $\bar{Z}_C^{\text{fit}} = 3.3$ . For comparison, the density-weighted average temperature and carbon ionization at this time, obtained from the HYDRA simulation, are  $\langle T \rangle_{\text{elec}} = 72 \text{ eV}$  and  $\langle \bar{Z}_C^f \rangle_{\text{elec}} = 3.8$ . The contours are determined from the cumulative  $\chi^2$  probability density function and define the regions of  $\bar{Z}_C^f - T$  space that can be fitted to the specified level of confidence. The boundaries of the 99.9% contour then serve to estimate the uncertainty in the temperature ( $\sim \pm 15\%$ ) and mean carbon ionization ( $\sim \pm 5\%$ ) to the aforementioned confidence. The greater relative sensitivity of the fit to the carbon ionization is not unexpected given the important role of bound electrons in the regions which contribute

most strongly to the scattering. However, varying either fitting parameter independently within the level of uncertainty shows that clear deviations from the optimum fit can be distinguished (see Fig. 7(b)).

We find that 0D fitting of the synthetic experimental data yields an estimate of the electron density-weighted average temperature that is within the demonstrated uncertainty. However, the fit underestimates the equivalent average ionization outside of the uncertainty. Since opacity effects have been effectively removed as a source of error from the fitting procedure, this suggests that the plasma gradients, which are not accounted for in the 0D model, are the source of this discrepancy. Such a result illustrates the importance of detailed modelling of XRTS from such highly nonuniform, dense plasmas. Furthermore, it shows that the gradients in the sampled volume must be carefully controlled if XRTS is to be used to make measurements which are correlated with physically meaningful conditions in our experiment.

## VII. DISCUSSION

The analysis presented in this work demonstrates the sensitivity of the scattering signal to regions of high density at large radii. If the scattered signal is uncollimated, we find that the temperature and mean charge state as determined by XRTS measurements to be heavily influenced by the conditions in the bulk of the shocked plasma behind the ablation front. To mitigate the issues associated with plasma gradients and opacity, and also to preferentially probe conditions near the compressed core of the target, we consider several modifications to the existing platform:

1. A revised ‘two-shock’ pulse shape has been proposed in order to produce a smoothly decreasing density profile. This pulse shape is expected to achieve similarly high pressures in the core with less target mass at larger radii. Thus, the density peak in the ablator region (see Fig. 1(b)), which is chiefly responsible for the large uncertainties of our  $\chi^2$  analysis, will be mitigated.

2. The complexities of modelling the x-ray attenuation, and any resulting the impact of robust data analysis, could be further diminished by using a higher energy x-ray source, e.g. the molybdenum He- $\alpha$  line at 18 keV. This would also serve to lessen the decrease in the absolute scattered signal intensity. On the other hand, the number of photons recorded by the detector would be significantly decreased since the second order Bragg diffraction of the crystal must be used, resulting in lower signal-to-noise levels.

3. An important consideration for realistic data analysis of a typical high-efficiency crystal spectrometer is the spectral broadening resulting from the relatively large scattering source volume (source broadening). Since the spatial signal weighting is asymmetric due to opacity effects, the broadening recorded by the spectrometer will also be asymmetric. Moreover, different spatial regions

emit different scattering spectra. This additionally influences the source broadening and underlines the importance of covering the problem in three dimensions. To reduce the impact of these effects, the scattering diagnostic could be moved to the equatorial plane inside the NIF target chamber, where larger scattering angles can be realised. This modification would increase the spectral separation of Rayleigh and Compton scattering features, thus reducing the affect of the source broadening.

4. In order to better sample the core region, the x-ray entrance slit in the hohlraum wall could be replaced with a pin hole. Whilst this would limit the photon flux into the target, it would effectively collimate the x-rays toward the core.

5. Finally, We note that more uniform sample conditions could be created by imploding spherical shells instead of solid spheres, although at the expense of the peak pressure. Scattered from compressed shells have recently been successfully demonstrated using a direct drive configuration at the Omega laser<sup>59</sup>.

## VIII. SUMMARY

In summary, we have developed a robust numerical framework for modelling x-ray Thomson scattering (XRTS) from large-scale, high density plasmas produced by multiple converging shocks at the NIF. Our model accounts for the substantial gradients in temperature, density and ionization level produced by the passage of the shocks and the effect of the plasma opacity on the transport of the diagnostic probe. We show that the shape of the scattered spectrum is not strongly affected by the transport of the x-rays through the dense plasma, but the absolute signal decreases when opacity is considered, as expected.

We showed that fitting 0D calculations to synthetic experimental data produced by our 3D modelling yields a best fit temperature which is close to the electron density-weighted average given my radiation-hydrodynamic modelling. On the other hand, we find that the ionization state predicted by simple 0D fitting is significantly smaller than the equivalent density-weighted average. This is due to large plasma gradients leading to the convolution of scattering spectra from different regions of the target, and cannot easily be accounted for in a simple 0D model. In order to mitigate such difficulties, we suggest several modifications to the laser drive, x-ray source and experimental geometry. We expect that the modifications discussed will minimise the uncertainties associated with scattering from strongly inhomogeneous targets and optimise the platform for XRTS measurements.

## ACKNOWLEDGEMENTS

This work was performed with the assistance of Lawrence Livermore National Laboratory (LLNL) under

Contract DE-AC52-07NA27344 and supported by Laboratory Directed Research and Development (LDRD) grants 11-ER-050 and 13-ERD-073. RWF and DK acknowledge support from SSAA program Contract No. DE-FG52-06NA26212.

- <sup>1</sup>S.H. Glenzer, W. Rozmus, B.J. MacGowan, K.G. Estabrook *et al.*, Phys. Rev. Lett. **82**, 97 (1999).
- <sup>2</sup>S.H. Glenzer, W. Rozmus, V.Yu. Bychenkov, J.D. Moody *et al.*, Phys. Rev. Lett. **88**, 235002 (2002).
- <sup>3</sup>D.H. Froula, L. Divol, H.A. Baldis, R.L. Berger, *et al.*, Phys. Plasmas **9**, 4709 (2002).
- <sup>4</sup>J.S. Ross, S.H. Glenzer, J.P. Palastro, B.B. Pollock *et al.*, Phys. Rev. Lett. **104**, 105001 (2010).
- <sup>5</sup>H.J. Lee, P. Neumayer, J. Castor, T. Döppner *et al.*, Phys. Rev. Lett. **102**, 115001 (2009).
- <sup>6</sup>C. Fortmann, H.J. Lee, T. Döppner, R.W. Falcone *et al.*, Phys. Rev. Lett. **108**, 175006 (2012).
- <sup>7</sup>D. Kraus, J. Vorberger, D.O. Gericke, V. Bagnoud *et al.*, Phys. Rev. Lett. **111**, 255501 (2013).
- <sup>8</sup>S. White, G. Nersisyan, B. Kettle, T.W.J. Dzelzanis *et al.* High Energy Dens. Phys. **9**, 573 (2013).
- <sup>9</sup>A.J. Visco, R.P. Drake, S.H. Glenzer, T. Döppner *et al.*, Phys. Rev. Lett. **108**, 145001 (2012).
- <sup>10</sup>S.P. Regan, K. Falk, G. Gregori, P.B. Radha *et al.*, Phys. Rev. Lett. **109**, 265003 (2012).
- <sup>11</sup>J. Vorberger, D.O. Gericke, Th. Bornath and M. Schlenges, Phys. Rev. E **81**, 046404 (2010).
- <sup>12</sup>D.H. Froula, L. Divol, N.B. Meezan, S. Dixit *et al.*, Phys. Plasmas **14**, 055705 (2007).
- <sup>13</sup>G. Gregori, S.H. Glenzer, K.B. Fournier, K.M. Campbell *et al.*, Phys. Rev. Lett. **101**, 045003 (2008).
- <sup>14</sup>G. Gregori, S.H. Glenzer, W. Rozmus, R.W. Lee *et al.*, Phys. Rev. E **67**, 026412 (2003).
- <sup>15</sup>S.H. Glenzer and R. Redmer, Rev. Mod. Phys. **81**, 1625 (2009).
- <sup>16</sup>P. Neumayer, C. Fortmann, T. Döppner, P. Davis *et al.*, Phys. Rev. Lett. **105**, 075003 (2010).
- <sup>17</sup>C. Fortmann, A. Wierling and G. Röpke, Phys. Rev. E **81**, 026405 (2010).
- <sup>18</sup>K. Wünsch, P. Hilse, M. Schlenges and D.O. Gericke, Phys. Rev. E **77**, 056404 (2008).
- <sup>19</sup>V. Schwarz, B. Holst, Th. Bornath, C. Fortmann *et al.*, High Energy Density Physics **6**, 305 (2010).
- <sup>20</sup>K. Wünsch, J. Vorberger, G. Gregori and D.O. Gericke, EPL **94**, 25001 (2011).
- <sup>21</sup>G. Gregori, S.H. Glenzer and O.L. Landen, Phys. Rev. E **74**, 026402 (2006).
- <sup>22</sup>D.A. Chapman and D.O. Gericke, Phys. Rev. Lett. **106**, 165004 (2011).
- <sup>23</sup>I. Golovkin, J.J. MacFarlane, P. Woodruff, I. Hall *et al.*, High Energy Density Phys. **9**, 510 (2013).
- <sup>24</sup>C.A. Haynam, P.J. Wegner, J.M. Auerbach, M.W. Bowers *et al.*, Appl. Optics **46**, 3276 (2007).
- <sup>25</sup>A.L. Kritcher, T. Döppner, D. Swift, J. Hawreliak *et al.*, High Energy Dens. Phys. **10**, 27 (2014).
- <sup>26</sup>J.L. Kline, S.H. Glenzer, R.E. Olson, L.J. Suter *et al.*, Phys. Rev. Lett. **106**, 085003 (2011).
- <sup>27</sup>S.H. Glenzer, B.J. MacGowan, N.B. Meezan, P.A. Adams *et al.*, Phys. Rev. Lett. **106**, 085004 (2011).
- <sup>28</sup>O.L. Landen, J. Edwards, S.W. Haan, H.F. Robey *et al.*, Phys. Plasmas **18**, 051002 (2011).
- <sup>29</sup>M.M. Marinak, S.W. Haan, T.R. Dittich, R.E. Tipton *et al.*, Phys. Plasmas **5**, 1125 (1998).
- <sup>30</sup>M.M. Marinak, G.D. Kerbal, N.A. Gentile, O. Jones *et al.*, Phys. Plasmas **8**, 2275 (2001).
- <sup>31</sup>J. Sheffield, D.H. Froula, S.H. Glenzer and N.C. Luhmann, Jr., *Plasma Scattering of Electromagnetic Radiation* Academic Press (New York) 2011.
- <sup>32</sup>A. Pelka, G. Gregori, D.O. Gericke, J. Vorberger *et al.*, Phys. Rev. Lett. **105**, 265701 (2010).

- <sup>33</sup>T.G. White, J. Vorberger, C.R.D. Brown, B.J.B. Crowley *et al.*, Nature Sci. Rep. **2**, 889 (2012).
- <sup>34</sup>T. Ma, T. Döppner, R.W. Falcone, L. Fletcher *et al.*, Phys. Rev. Lett. **110**, 065001 (2013).
- <sup>35</sup>D. Swift, J. Hawrelak, D. Braun, A.L. Kritcher *et al.*, AIP Conf. Proc. **1426**, 477 (2012).
- <sup>36</sup>T. Döppner, A.L. Kritcher, S.H. Glenzer, B. Bachmann *et al.*, Submitted to J. Phys. Conf. Series (2014).
- <sup>37</sup>E. Fourkal, V. Yu. Bychenkov, W. Rozmus *et al.*, Phys. Plasmas **8**, 500 (2001).
- <sup>38</sup>J.L. Kline, D.S. Montgomery, B. Bezzerides, J.A. Cobble *et al.*, Phys. Rev. Lett. **94**, 175003 (2005).
- <sup>39</sup>R.R. Fäustlin, Th. Bornath, T. Döppner, S. Düsterer *et al.*, Phys. Rev. Lett. **104**, 125002 (2010).
- <sup>40</sup>D.A. Chapman, J. Vorberger, K. Wünsch and D.O. Gericke, High Energy Dens. Phys. **8**, 175 (2012).
- <sup>41</sup>S.H. Glenzer, W.E. Alley, K.G. Estabrook, J.S. de Groot *et al.*, Phys. Plasmas **6**, 2117 (1999).
- <sup>42</sup>Z. Wang, J. Zheng, B. Zhao, C.X. Yu *et al.* Physics of Plasmas **12**, 082703 (2005).
- <sup>43</sup>B. La Fontaine, J. Dunn, H.A. Baldis, G.D. Enright *et al.* Phys. Rev. E **47**, 583 (1993).
- <sup>44</sup>H.A. Baldis, J. Dunn, M.E. Foord and W. Rozmus, Rev. Sci. Instrum. **73**, 4223, (2002).
- <sup>45</sup>R. Thiele, P. Sperling, M. Chen, Th. Bornath *et al.* Phys. Rev. E **82** 056404 (2010).
- <sup>46</sup>S.H. Glenzer, K.G. Estabrook, R.W. Lee, B.J. MacGowan *et al.* J. Quant. Spectrosc. Rad. Trans. **65**, 253 (2000).
- <sup>47</sup>W. Rozmus, S.H. Glenzer, K.G. Estabrook, H.A. Baldis *et al.* Astrophys. J. Suppl. Series **127**, 459 (2000).
- <sup>48</sup>C. Fortmann, R. Thiele, R.R. Fäustlin, Th. Bornath *et al.* High Energy Dens. Phys. **5**, 208 (2009).
- <sup>49</sup>B.J.B. Crowley and G. Gregori, New J. Phys. **15**, 015014 (2013).
- <sup>50</sup>J. Chihara, J. Phys.: Condens. Matter **12**, 231 (2000).
- <sup>51</sup>G. Gregori, S.H. Glenzer, H.-K. Chung, D.H. Froula *et al.*, J. Quant. Spectrosc. Rad. Trans. **99**, 225 (2006).
- <sup>52</sup>G. Gregori and D.O. Gericke, Phys. Plasmas **16**, 056306 (2009).
- <sup>53</sup>J. Vorberger, Z. Donko, I.M. Tkachenko and D.O. Gericke, Phys. Rev. Lett. **109**, 225001 (2012).
- <sup>54</sup>F.J. Rogers, F.J. Swenson and C.A. Iglesias, Astrophys. J. **456**, 902 (1996).
- <sup>55</sup>D. Kremp, M. Schlages and W.-D. Kraeft, *Quantum Statistics of Nonideal Plasmas*, Springer (Berlin) 2005.
- <sup>56</sup>A. Selchow, G. Röpke, A. Wierling, H. Reinholz *et al.*, Phys. Rev. E **64**, 056410 (2001).
- <sup>57</sup>M. Schumacher, F. Smend and I. Borchert, J. Phys. B: Atom. Molec. Phys. **8**, 1428 (1975).
- <sup>58</sup>G. Gregori, S.H. Glenzer, F.J. Rogers, S.M. Pollaine *et al.* Phys. Plasmas **11**, 2754 (2004).
- <sup>59</sup>L.B. Fletcher, A.L. Kritcher, A. Pak, T. Ma *et al.*, Phys. Rev. Lett. **112**, 145004 (2014).
- <sup>60</sup>B.A. Mattern and G.T. Seidler, Phys. Plasmas **20**, 022706 (2013).
- <sup>61</sup>K. Wünsch, J. Vorberger and D.O. Gericke, Phys. Rev. E **79**, 010201(R) (2009).
- <sup>62</sup>L. Pauling and J. Sherman, Zeitschr. Kristallogr. **81**, 1 (1932).
- <sup>63</sup>D.O. Gericke, J. Vorberger, K. Wünsch and G. Gregori, Phys. Rev. E **81**, 065401(R) (2010).
- <sup>64</sup>D.A. Chapman, J. Vorberger, L.B. Fletcher, L. Divol *et al.*, Submitted (2014).
- <sup>65</sup>T.R. Boehly, R.S. Craxton, T.H. Hinterman, J.H. Kelly *et al.*, Rev. Sci. Instrum. **66**, 508 (1995).
- <sup>66</sup>J.A. Gaffney, D. Clark, V. Sonnad and S.B. Libby, High Energy Density Physics **9**, 457 (2013).
- <sup>67</sup>J.A. Gaffney, D. Clark, V. Sonnad and S.B. Libby, Nucl. Fusion **53**, 073032 (2013).
- <sup>68</sup>Y. Avni, Astrophys. J. **210**, 642 (1967).